Available online at www.sciencedirect.com
SCIENCE DIRECT®
International Journal of Heat and Mass Transfer 47 (2004) 229–243
International Journal of HEAT and MASS TRANSFER
www.elsevier.com/locate/ijhmt

# Heat transfer in rectangular channels with transverse and V-shaped broken ribs

Giovanni Tanda *

*Dipartimento di Termoenergetica e Condizionamento Ambientale (DITEC), Università degli Studi di Genova, Via all'Opera Pia 15/a, I-16145 Genova, Italy*

Received 3 April 2003; received in revised form 15 July 2003

**Abstract**

Repeated ribs are used on heat exchange surfaces to promote turbulence and enhance convective heat transfer. Applications include fuel rods of gas-cooled nuclear reactors, inside cavities of turbine blades, and internal surfaces of pipes used in heat exchangers. Despite the great number of literature papers, only few experimental data concern detailed distribution of the heat transfer coefficient in channels with rib turbulators. This issue was tackled by means of the steady-state liquid crystal thermography: a pre-packaged liquid crystal film was glued onto the heated surface, and the colour map was taken by a video camera at the steady state of a given experiment. After calibration tests to assess the colour–temperature relationship had been performed, local heat transfer coefficients were obtained by applying custom-made software to process the digitised colour images. Liquid crystal thermography was applied to the study of heat transfer from a rectangular channel (width-to-height ratio equal to five) having one surface heated at uniform heat flux and roughened by repeated ribs. The ribs, having rectangular or square sections, were deployed transverse to the main direction of flow or V-shaped with an angle of 45 or 60 deg relative to flow direction. The effect of continuous and broken ribs was also considered. Local heat transfer coefficients were obtained at various Reynolds numbers, within the turbulent flow regime. Area-averaged data were calculated in order to compare the overall performance of the tested ribbed surfaces and to evaluate the degree of heat transfer enhancement induced by the ribs with respect to the smooth channel.


## 1. Introduction

Rib arrays inside internal channels are often used in heat exchanger systems to enhance the heat transfer rate. A typical application is the internal cooling of gas turbine blades: the ribs break the laminar sublayer and create local wall turbulence due to flow separation and reattachment between the ribs, thus greatly enhancing the cooling effect.

First studies dealt with uniformly heated tubes and square or rectangular channels with rib-roughened walls; continuous, regularly spaced, transverse ribs have been the most common ribbed geometry for years [1–4]. The effects of the most important parameters (rib height $e$, rib pitch $p$, channel aspect ratio $AR$, hydraulic diameter $D$, and Reynolds number $Re$) on heat transfer and pressure drop were investigated in detail. These studies showed that the heat transfer coefficient (as well as the pressure drop) attains a maximum value for $p/e = 6$–$15$ (in turn depending on $e/D$ and $Re$) and increases with $e/D$ (in the explored range from 0.004 to 0.063). The existence of an optimum value of $p/e$ is due to the fact that, at small $p/e$, the flow which separates after each rib does not reattach close to the next rib, while for large $p/e$ the reattachment point is reached and a boundary layer begins to grow before the succeeding rib is encountered, reducing both the average shear stress and the heat transfer.

Further studies [5–11] showed that parallel angled ribs provide a better heat transfer performance than transverse ribs because of the secondary flow induced by the rib angle. In particular, superior heat transfer

* Tel.: +390-10-353-2881; fax: +390-10-311-870.
*E-mail address:* tanda@ditec.unige.it (G. Tanda).

0017-9310/$ - see front matter © 2003 Elsevier Ltd. All rights reserved.
doi:10.1016/S0017-9310(03)00414-9

**Nomenclature**

| | |
|---|---|
| $A$ | heated surface area |
| $AR$ | channel aspect ratio, $W/H$ |
| $c_p$ | specific heat (at constant pressure) of air |
| $D$ | channel hydraulic diameter of the rectangular channel, $2WH/(W+H)$ |
| $d$, $d'$ | geometric parameters of broken ribs |
| $e$ | rib height |
| $f$ | Fanning friction factor, $(\Delta P/L')D\rho/(2G^2)$ |
| $f_0$ | Fanning friction factor for the reference (unribbed) channel |
| $k$ | thermal conductivity of air |
| $G$ | air mass velocity, $m'/(WH)$ |
| $H$ | channel height |
| $h$ | convective heat transfer coefficient |
| $L$ | length of heated surface |
| $L'$ | distance between the pressure taps |
| $l$, | rib length |
| $m'$ | air mass flow rate |
| $Nu$ | local Nusselt number |
| $Nu_{av}$ | area-averaged Nusselt number |
| $Nu_0$ | Nusselt number for the fully developed flow in the reference (unribbed) channel |
| $Pr$ | Prandtl number |
| $P$ | pressure |
| $p$ | rib pitch |
| $q_{conv}$ | convective heat flux |
| $Q_{el}$ | input power to the heater |
| $Q_{rad}$ | radiation heat transfer rate |
| $Q_{dis}$ | conduction heat transfer rate |
| $Q_{ribs}$ | heat transfer rate from ribs |
| $Re$ | Reynolds number, $GD/\mu$ |
| $Re_0$ | Reynolds number for the reference channel |
| $T_{LC}$ | surface temperature (by liquid crystals) |
| $T_{air,x}$ | air bulk temperature |
| $T_{air,0}$ | inlet air temperature |
| $W$ | channel width |
| $x$ | longitudinal coordinate |

*Greek symbols*

| | |
|---|---|
| $\alpha$ | rib angle-of-attack |
| $\rho$ | density of air |
| $\mu$ | dynamic viscosity of air |

performance per unit friction expenditure can be potentially achieved. In annular flow, White and Wilkie [5] found that angling the ribs causes both heat transfer coefficient and pressure drop to decrease; however, friction factor $f$ decreases faster than Nusselt number $Nu$ and therefore a 33 deg helix angle with $p/e = 8$ showed the greatest gain in performance, per unit pumping power, over that of a zero helix angle (i.e. a transverse rib). In parallel-plate flow (i.e. very large $AR$ values), Han et al. [6] concluded that as the angle-of-attack changes from 90 to 45 deg with $p/e = 10$–20 and $e/D = 0.102$, $Nu$ decreases only by 5% despite the larger reduction in $f$: an angle near 45 deg was then deemed as the more appropriate for optimum thermal-hydraulic performance. In successive studies [7–9], Han and coworkers found that in a uniformly heated square channel ($AR = 1$) ribbed on two opposite sides and smooth on the other sides, with $p/e = 10$–20 and $e/D = 0.063$, the highest $Nu$, accompanied by the highest $f$, occurred at rib angles of attack between 60 and 75 deg, whereas the best performance for a constant pumping power occurred at an angle-of-attack between 30 and 45 deg. For rectangular channels ($p/e = 10$–20 and $e/D = 0.047$–0.078) with large aspect ratio ($AR = 2$ or 4, ribbed on the larger sides), it was found that angling the ribs has a little impact on heat transfer performance, while the rib angle effect is important for the narrow aspect ratio channels ($AR = 1/2$ and 1/4). In circular tube flow, Gee and Webb [10] and Sethumadhavan and Raja Rao [11] reported that the best performance was identified with $p/e = 10$–15 at the rib angle of attack of about 50–60 deg.

In order to promote higher levels of flow turbulence, further experiments were performed by displacing the angled ribs according to a crossed arrangement or a V-shaped arrangement with the apex of V pointing upstream or downstream [12–14]. Results presented by Han et al. [12], again for a square channel ($AR = 1$) ribbed on two opposite sides, $e/D = 0.0625$, $p/e = 10$ and $Re = 15{,}000$–$90{,}000$, showed that the 45–60 deg V-shaped ribs perform better than the 45–60 deg parallel angled ribs, the 45–60 deg angled crossed ribs and the parallel transverse ribs, in sequence. Since the orientation of the angled leg of V-shaped ribs induce different types of secondary flows and different distributions of the local heat transfer coefficient as found in [13], it is interesting to note that in [12] the V-shaped ribs performed better when pointing upstream, while more recently, Gao and Sundén [14] found that, for a rectangular ($AR = 8$) channel ribbed on both sides, with $e/D = 0.06$, $p/e = 10$ and $Re = 1000$–$6000$, 60 deg V-shaped ribs produced higher heat transfer enhancement when pointing downstream of the main flow direction (rather than upstream), seemingly contradicting results of [12].

The next step, aimed at achieving even more efficient rib displacements from the heat transfer point of view,

consisted in interrupting the continuity of ribs, on the ground that broken V-shaped or parallel ribs can create more secondary flow cells and produce more local turbulence than the continuous V-shaped or parallel ribs. Han and Zhang [15] found that in a uniformly heated, square channel with $e/D = 0.0625$, $p/e = 10$ and $Re =$ 15,000–90,000 the 60 deg, V-shaped, broken ribs offered higher heat transfer enhancement than other broken and continuous, parallel and V-shaped rib configurations, while the 90 deg broken ribs produced the largest pressure drop. The effect of 60 deg, broken V ribs was also tested in two-pass square channels by Ekkad and Han [16]. More recently, Liou et al. [17] obtained detailed local Nusselt number distributions induced by single obstructions (ribs or delta winglets) on one surface of a square channel ($e/D = 0.012$, $Re = 12{,}000$). Among the different configurations, including continuous ribs (transverse, angled and V-shaped) and broken 60 deg, V-shaped ribs, the highest local heat transfer enhancements (up to a 3.7 factor) are induced by the 45 deg, continuous, V shaped ribs). Cavallero and Tanda [18] investigated local and average heat transfer characteristics for continuous and broken transverse ribs ($e/D = 0.15$, $p/e = 4$ and 8, with a different definition of $p$ for broken ribs with respect to [15], $Re = 9000$–$35{,}000$) placed over one side of a rectangular channel ($AR = 5$), finding again marked heat transfer augmentations (relative to a smooth channel) when ribs are interrupted.

Inspection of the literature reveals that further investigations are required, especially for local heat transfer distributions in the presence of broken ribs with different arrangements (transverse, parallel angled and V-shaped). Moreover, since the use of broken ribs increases both heat transfer and friction, evaluation criteria have to be developed to demonstrate the performance advantage relative to smooth passages of equal hydraulic diameter.

An important aspect in experimental heat transfer tests in ribbed channels is the adopted measuring technique. A number of investigations have been performed by the standard, heater plates/foils and thermocouple technique [1,3–12,15] or the naphthalene sublimation technique [2,13], both experimental methods providing accurate but discrete, or regionally averaged, results. In general, detailed maps of the local heat transfer coefficient can be obtained by using optical techniques, such as the infra-red thermographic technique [19] and the (steady or transient) liquid crystal (LC) technique [14,16–18]. Despite the large amount of information gained by these thermographic methods, experimental studies of heat transfer in ribbed channels are still less numerous than those performed by the standard thermocouple technique. In particular, LC techniques, more economical and affordable than the infrared thermal imaging method, can be classified into two categories: the steady method and the transient method. The steady LC method allows the entire surface to be mapped from one LC image using a colour processing system. To overcome the problem of limited colour play range, the heat flux into the surface can be adjusted in order to move the colour band to different locations and so progressively map the heat transfer coefficient over the entire test section. The transient LC method is based on the fact that when the test surface of a uniform initial temperature is suddenly exposed to a uniformly heated or cooled flow, the magnitudes of the time-varying surface temperature is governed by transient heat conduction penetrating into a semi-infinite solid (see, for instance, Ref. [16]). An alternative transient LC method consists in employing a thin plastic sheet as the test surface, thus ignoring the thermal gradient in the material, with the local surface temperature depending on time only [20]. Despite the experimental difficulty to produce a uniform flux density, steady-state methods are conceptually simpler and easier to analyse than the transient methods, which require a more complicated image processing system (several image acquisitions per second are required to detect the time elapsed to arrive locally at a given temperature). On the other hand, Valencia et al. [20] found that neglecting tangential conduction is more critical for steady-state experiments, even though they performed comparative tests at a relatively low Reynolds number ($Re = 500$).

In this paper, local and average heat transfer coefficients in a rib-roughened rectangular channel (aspect ratio $AR$ equal to 5) are presented. Configurations including sequences of transverse continuous, transverse broken and V-shaped broken ribs have been considered. Ribs have square or rectangular cross-sections (rib height $e = 3$ or 5 mm) and are regularly spaced, over the uniformly heated side of the channel (the other sides remaining smooth and unheated), by a rib pitch $p = 40$ mm, so as to yield two values of the pitch-to-rib height ($p/e = 8$ and 13.3), the Reynolds number $Re$ ranging from 8900 to 36,000. Ribs, made of Plexiglas, were considered to be nearly adiabatic for the thermal boundary condition; therefore attention was focused on local and average heat transfer coefficients on the heated endwall plate. The study was performed by using the steady-state liquid crystal technique.

## 2. Experimental apparatus and procedure

### 2.1. Experimental setup

The description of the experimental apparatus is facilitated by reference to Fig. 1. The main components are the wind tunnel, the test section, the heating arrangement, and the instrumentation. An open-circuit suction-type wind tunnel was used for this study. Air, drawn at room temperature, passed through a filter and

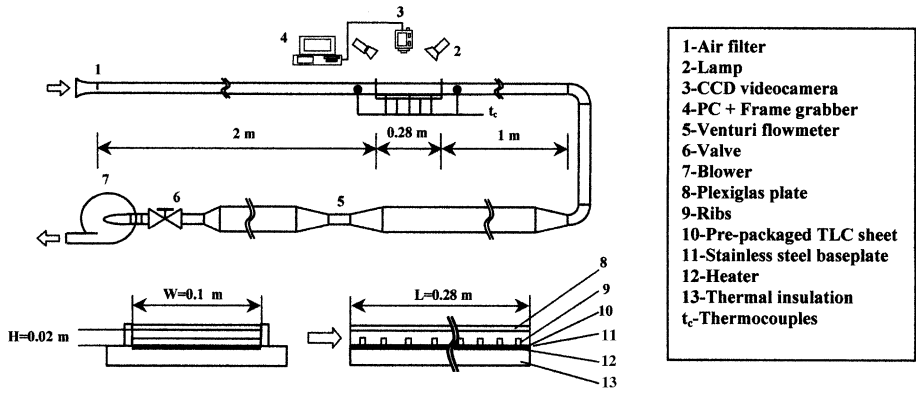


Fig. 1. Experimental apparatus: schematic diagram and test section details.

entered a rectangular channel (width $W = 0.1$ m, height $H = 0.02$ m, aspect ratio $W/H = 5$, hydraulic diameter $D = 0.033$ m) in which the test section was fitted. The rectangular channel consisted of a hydrodynamic development section, the test section, and the exit section. This duct was followed by a long circular pipe which contained a control valve and a Venturi flowmeter and terminated at the blower inlet. The air discharged from the blower was ducted out of the laboratory room.

The test section was a rectangular channel, as wide and high as the entry and exit sections and delimited by a thin heated plate (0.1 m wide and 0.28 m long) and lateral and frontal Plexiglas walls. The plate was made of 0.5 mm thick stainless steel to which a plane heater had been attached to provide a controllable uniform heat flux. A thin liquid crystal sheet was applied on the side opposite to the heater to measure local wall temperature. The side walls of the test section were covered with thermal insulation layers in order to convey as much as possible of the electric power dissipated by the heater to the convective air flow. Power was supplied by an adjustable DC source and measured by a voltmeter and an amperometer. Fine-gauge thermocouples were placed inside the rectangular channel directly exposed to the airflow and in several places inside the channel wall material. These sensors were used to measure the air temperature at the test section inlet, estimate conduction heat losses to the surroundings, and control the attainment of the steady-state conditions. Pressure taps, connected to a common alcohol manometer, were located at the inlet and outlet of the test section in the streamwise direction. A Venturi flowmeter was used for the measurement of mass flow rate.

Thermosensitive, cholesteric liquid crystals were used to measure temperature distributions on the heated surface. The pre-packaged liquid crystal sheet (0.15 mm thick) consisted of a thermochromic liquid crystal layer on a black background applied onto a mylar film and backed with a pressure-sensitive adhesive. The colour distribution of the liquid crystals was observed by a CCD videocamera through the Plexiglas wall opposite to the heated surface and stored in a PC equipped with a frame grabber. Four 100 W lamps were used to illuminate the test section during image storing. The lamps were switched on only for the time strictly required for image acquisition, to prevent radiant heating of the test surface.

### 2.2. Rib configurations

Ribs were made of Plexiglas and glued onto the heated plate. They had either a rectangular ($5 \times 3$ mm$^2$) or a square section ($3 \times 3$ mm$^2$). Owing to their low thermal conductivity, the ribs were considered to be virtually adiabatic and their function was to generate turbulence in the airflow in order to increase the endwall heat transfer. Seven rows of rib elements, continuous and interrupted, were arranged transverse or inclined (V-shaped) with respect to the main flow direction, at periodic streamwise stations (rib pitch $p = 40$ mm), as shown in Fig. 2. Table 1 lists the rib configurations studied: continuous transverse ribs (**1-I** and **1-II**), 90 deg broken ribs (**2-I** and **2-II**), 60 deg (**3-I** and **3-II**) and 45 deg (**4-I** and **4-II**) V-shaped, broken ribs; for each of them two values of the rib height $e$ were considered (5 and 3 mm), giving a rib pitch-to-height ratio ($p/e$) equal to 8 and 13.3, respectively, and a rib-to-channel height ratio ($e/H$) equal to 0.25 and 0.15, respectively. The open space $d'$ between adjacent broken ribs (in the transverse direction) was the same for the **2-3-4** broken rib arrangements, so as to provide the same frontal flow area at the same $e/D$ value. For the purpose of comparison, average heat transfer coefficients and pressure drop for rib configurations (continuous transverse ribs **1-#** and 90 deg broken ribs **5-#**) reported in [18] are included, while the relevant local heat transfer results were omitted here, since they are documented in detail in [18].

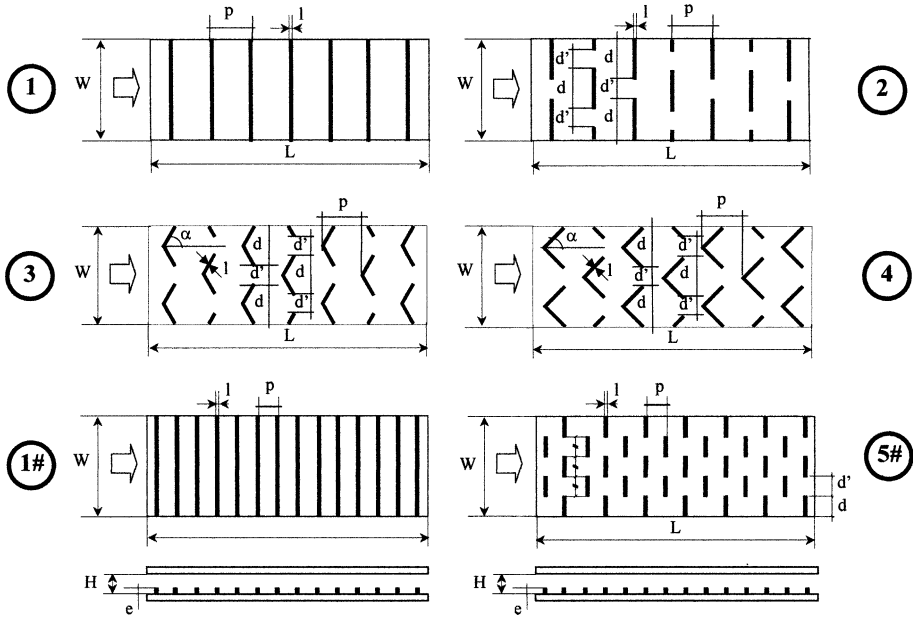


Fig. 2. Geometry of rib configurations studied: **1**. Transverse continuous ribs (I,II), **2**. Transverse broken ribs (I,II). **3**. Broken 60 deg V-ribs (I,II). **4**. Broken 45 deg V-ribs (I,II). **1-#**. Transverse continuous ribs. **5-#**. Transverse broken ribs. (I, II and # denote different rib pitch-to-height ratios).

Table 1
Geometric characteristics of rib configurations

| Configuration | $e$ (mm) | $l$ (mm) | $\alpha$ (deg) | $d$ (mm) | $d'$ (mm) | $e/D$ | $p/e$ | $e/H$ |
|---|---|---|---|---|---|---|---|---|
| **1-I** continuous ribs | 5 | 3 | 90 | – | – | 0.15 | 8 | 0.25 |
| **2-I** broken ribs | 5 | 3 | 90 | 40 | 20 | 0.15 | 8 | 0.25 |
| **3-I** broken V-ribs | 5 | 3 | 60 | 40 | 20 | 0.15 | 8 | 0.25 |
| **4-I** broken V-ribs | 5 | 3 | 45 | 40 | 20 | 0.15 | 8 | 0.25 |
| **1-II** continuous ribs | 3 | 3 | 90 | – | – | 0.09 | 13.3 | 0.15 |
| **2-II** broken ribs | 3 | 3 | 90 | 40 | 20 | 0.09 | 13.3 | 0.15 |
| **3-II** broken V-ribs | 3 | 3 | 60 | 40 | 20 | 0.09 | 13.3 | 0.15 |
| **4-II** broken V-ribs | 3 | 3 | 45 | 40 | 20 | 0.09 | 13.3 | 0.15 |
| **1-#** continuous ribs[a] | 5 | 3 | 90 | – | – | 0.15 | 4 | 0.25 |
| **5-#** broken ribs[a] | 5 | 3 | 90 | 20 | 20 | 0.15 | 4 | 0.25 |

[a] Local heat transfer results reported in Ref. [18].

### 2.3. Calibration of thermosensitive liquid crystals

The relationship between the colour and temperature of the thermosensitive liquid crystals (LC) was found by a calibration experiment. The calibration test was carried out by gradually heating a 5 mm thick aluminium plate (calibration plate) covered by a liquid crystal film identical to that used in the experiments. The calibration plate was placed in the test section and equipped with ten fine-gauge type-K thermocouples calibrated to ±0.1 K. The thermocouples, housed in small holes drilled in the material at different positions as close to the surface as possible, were used to measure the wall temperature and the degree of surface temperature uniformity. The inlet and outlet passages of the test section were blocked during the calibration test in order to promote isothermal conditions inside the test section. For a given wall temperature, the corresponding colour image displayed by the liquid crystals was digitised and processed in order to obtain, pixel by pixel, the HSI (hue, saturation, intensity) contents from the RGB (red, green, blue) domain. Among the new parameters (H,S,I) only hue was retained since it was found to be the only one correlated with the surface temperature [21]. The hue-temperature correlation of calibration data is reported in Fig. 3 and depends not only on the type of liquid crystals but also on the recording angle, and on the features of the illumination and of the test section (presence of transparent or reflecting walls). The hue-temperature correlation was found to be fairly linear and repeatable in the range from 30.5 to 32.5 °C,

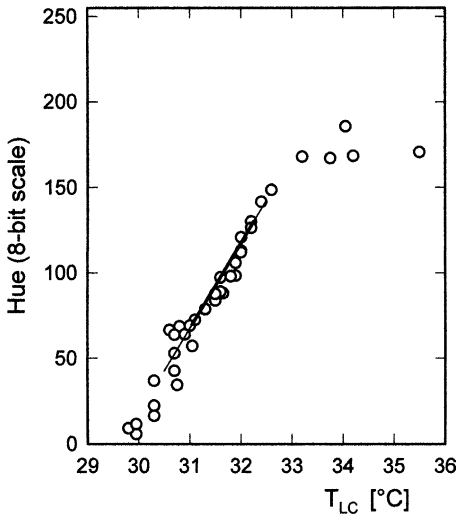


Fig. 3. Hue-temperature calibration with regression line.

corresponding to the range of hue (expressed on an eight-bit integer scale) between 42.5 and 142.5. Regression of data turned out to be particularly accurate in the 70–130 hue range (31–32.2 °C): this field of hue was therefore selected for the quantitative analysis of each LC image. The corresponding calibration line has an uncertainty band (at the 95% confidence interval) of ±0.2 K. In order to minimise the hysteresis phenomena detected by Baughn et al. [22], care was taken to avoid reaching very high temperatures (say higher than 40 °C) on the test surface in relation to the LC working temperature.

### 2.4. Operating procedure and data reduction

After the rib array had been set and the airflow had been adjusted to a prescribed velocity, the DC current was supplied to the heater. The surface temperature was maintained within the thermosensitivity region of the liquid crystals by controlling the input power delivered to the heater. Once steady-state conditions were reached, input power, thermocouple readings and the liquid crystal images were recorded. The image of the coloured pattern of liquid crystals was taken by the CCD videocamera and converted by the frame grabber to a BMP file, for subsequent manipulation by standard graphical packages and by the algorithm for the RGB to HSI pixel-by-pixel conversion. A convolution filter was used to minimise the effects of image defects producing, in isolated pixels, values of hue not correlated to the surface temperature. The final step consisted in applying custom-made software to convert the hue into the surface temperature in order to extract the local heat transfer coefficient according to the following relationship:

$$h = q_{\mathrm{conv}}/(T_{\mathrm{LC}} - T_{\mathrm{air},x}) \tag{1}$$

where $q_{\mathrm{conv}}$ is the convective heat flux, assumed to be uniformly distributed over the heated plate, $T_{\mathrm{LC}}$ is the surface temperature detected by the liquid crystals and $T_{\mathrm{air},x}$ is the bulk temperature of the air at the $x$ position along the streamwise direction.

The convective heat flux was evaluated as follows:

$$q_{\mathrm{conv}} = (Q_{\mathrm{el}} - Q_{\mathrm{rad}} - Q_{\mathrm{dis}} - Q_{\mathrm{ribs}})/A \tag{2}$$

where $Q_{\mathrm{el}}$ is the measured input power to the heater, $Q_{\mathrm{rad}}$ is the calculated radiative heat transfer rate to the surroundings, $Q_{\mathrm{dis}}$ is the calculated heat transfer rate dissipated through the insulation on the rear face of the heater, and $A$ is the area of the plate surface exposed to the airflow. The term $Q_{\mathrm{ribs}}$ takes into account the heat dissipation from the ribs. Even though the ribs were deemed to be adiabatic owing to their low thermal conductance, the conventional one-dimensional fin model was applied to estimate the small amount of heat transfer rate delivered to the airflow from their sides. If the heat transfer coefficient along the rib is assumed to be equal to the average heat transfer coefficient over the baseplate, $Q_{\mathrm{ribs}}$ calculated by an iterative procedure is generally less than 7% of $Q_{\mathrm{el}}$ while the sum of $Q_{\mathrm{rad}}$ and $Q_{\mathrm{dis}}$ was always found to be within 5–11% of $Q_{\mathrm{el}}$.

The bulk temperature of air at the $x$-position was calculated by the following equation:

$$T_{\mathrm{air},x} = T_{\mathrm{air},0} + (Q_{\mathrm{el}} - Q_{\mathrm{dis}} - Q_{\mathrm{rad}})(x/L)/(m' c_p) \tag{3}$$

where $T_{\mathrm{air},0}$ is the air temperature measured at the entrance of the test section (where the flow is isothermal), $c_p$ is the air specific heat, $m'$ is the mass flow rate and $L$ is the heated surface length.

The convective heat flux $q_{\mathrm{conv}}$ varied from about 400 to 1800 W/m$^2$ depending on the test conditions; air temperature rises along the test section were typically within 2 K in the presence of average plate-to-air temperature differences of about 8–13 K.

As previously explained, only points having the hue within the 70–130 range are processed; outside the selected hue interval, no information is gained; therefore, in those cases, tests were repeated at the same air flow rate and for 3–5 different values of the input power (typically varying the input power by ±20%), this in order to move the colour pattern toward the regions not previously monitored and to locally extract the values of the heat transfer coefficient. Another important issue is the resolution of the liquid crystal images. When the whole test section is pictured inside a single image, after digitising and filtering processes the resolution is about 0.87 mm/pixel. This can be enhanced by increasing the magnification of the videocamera (up to 0.31 mm/pixel) but in this case only a reduced region of the test surface is framed and numerous images therefore have to be stored and linked in order to reconstruct the heat transfer coefficient over the entire test surface. Since this last procedure is

lengthy and demanding, the majority of image acquisitions in this study were obtained from full-field pictures.

Experimental data were recast in dimensionless form, introducing the Nusselt number $Nu$ and the Reynolds number $Re$ as follows:

$$Nu = hD/k \tag{4}$$

$$Re = GD/\mu \tag{5}$$

where $G = m'/(WH)$ is the air mass velocity in the channel (air mass flow rate per unit area) and $D = 2WH/(W + H)$ is the channel hydraulic diameter.

To obtain a dimensionless representation of the pressure drop due to the ribs, the friction factor $f$, based on adiabatic conditions (i.e., test without heating), was introduced according to the Fanning definition:

$$f = (\Delta P/L')D\rho/(2G^2) \tag{6}$$

where $L'$ is the axial distance between the two pressure taps, approximately equal to the test section length $L$. Thermal conductivity $k$, dynamic viscosity $\mu$ and density $\rho$ of air were evaluated at the film temperature.

Uncertainty analysis was performed by applying the estimation method proposed by Moffat [23]. The uncertainty (at the 95% confidence level) in local $h$ values was estimated to be ±5.6%. This value takes into account the effects of measuring errors in voltage, current and LC thermographic readings and of thermal conduction, along transverse and longitudinal directions, inside the stainless steel, heated plate. The Reynolds number had a calculated uncertainty of ±3.2%. Finally, the uncertainty in the friction factor $f$ was estimated to be ±7.8% at the lowest Reynolds numbers and 3.4% at the highest Reynolds numbers.

## 3. Results and discussion

### 3.1. Local heat transfer characteristics

Fig. 4 shows a typical map of heat transfer coefficients over the whole ribbed surface (280×100 mm), from which some information can be obtained such as heat transfer coefficient (or Nusselt number) distributions along any transverse and longitudinal section, spanwise-averaged and regionally (over a module or the total area) averaged heat transfer coefficients. In order to infer local heat transfer features for the investigated rib configurations, attention was focused on the distributions of the Nusselt number along the centerline (dashed-dotted line in Fig. 4) and over the central region of the heated surface (80 mm long, 60 mm wide, inline region in Fig. 4).

Local Nusselt number $Nu$ along the centerline for the transverse, continuous ribs is shown in Fig. 5 ($Re = 8900$ and 28,500). Vertical lines correspond to the surface interruptions due to ribs spaced 40 mm along the $x$-coordinate. A periodic inter-rib $Nu$-distribution is reached about after 2–3 repetitive modules (i.e. after 3–4 ribs), indicating the attainment of a periodic, fully developed, thermal region. This results is consistent with Ref. [4], indicating $x/D_{ch} > 3$ for the settlement of a periodic pattern. The typical inter-rib $Nu$-distribution reaches a maximum value, probably at the point of flow reattachment (approximately after 4 rib heights downstream from separation, as found in [4]). Downstream of the reattachment point, the heat transfer coefficient decreases up to the vicinity of the successive rib, where the flow separation near the corner between the endwall and the rib leads to a further increase in the heat transfer coefficient. The thermal boundary layer growing downstream of the reattachment point is responsible for the more pronounced decrease of the heat transfer coefficient beyond the relative maximum found for $p/e = 13.3$.

Transverse broken ribs, in a staggered arrangement, lead to higher levels of turbulence over the heated surface, as shown in Fig. 6 where the heat transfer distributions along the centerline are plotted. Inspection of the figure reveals that local heat transfer is enhanced, relative to continuous ribs, and especially for $p/e = 8$. The inter-rib $Nu$-distributions still show a relative maximum between ribs but values recorded at periodically

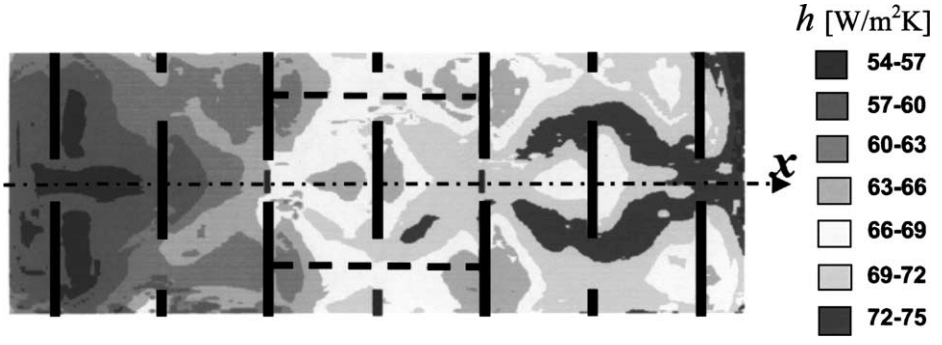


Fig. 4. Map of heat transfer coefficients (W/m$^2$ K) for the 90 deg broken rib configuration 2-I ($Re = 8900$).

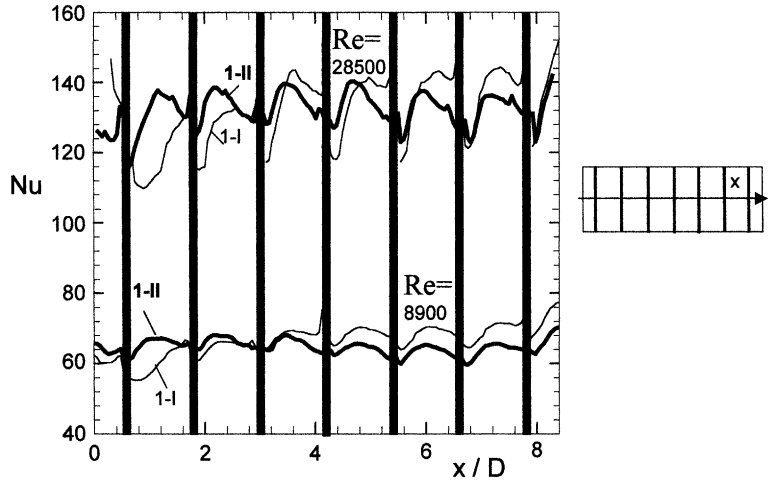


Fig. 5. Distributions of center-line Nusselt number for the transverse, continuous rib configurations 1-I ($p/e = 8$) and 1-II ($p/e = 13.3$), for $Re = 8900$ and 28,500.

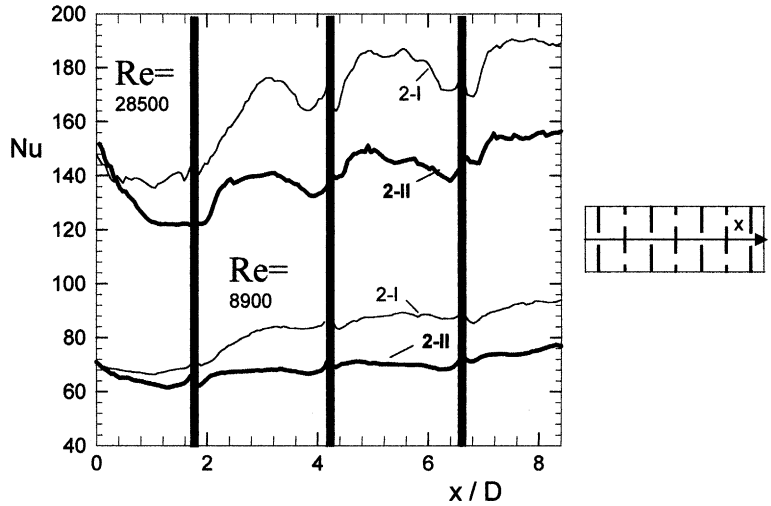


Fig. 6. Distributions of center-line Nusselt number for the transverse (90 deg) broken rib configurations 2-I ($p/e = 8$) and 2-II ($p/e = 13.3$), for $Re = 8900$ and 28,500.

positioned sites tend to increase from the entrance to the exit, thus denoting incompletely developed thermal conditions.

When ribs are V-shaped and broken, the features of the centerline *Nu*-distributions, plotted in Figs. 7 and 8, depend on $p/e$ and the shape angle. The inter-rib *Nu*-profiles for 60 deg V-ribs (Fig. 7) are characterised, for $p/e = 8$ ($e = 5$ mm), by only slight reductions in *Nu* as the relative maximum (here 5–6 rib heights downstream from the V apex) is reached. At the higher rib pitch to height ratio ($p/e = 13.3$, $e = 3$ mm), *Nu* increases up to a relative maximum, approximately located at 3–5 rib heights downstream from ribs, and then markedly decreases, denoting the presence of a large region poorly active from the heat transfer point of view. The inter-rib distributions for 45 deg V-ribs (Fig. 8) clearly show a relative maximum (approximately 4–5 rib heights downstream from the V apex) followed by a marked reduction, for both $p/e$ values. Increasing levels of heat transfer coefficients at periodically spaced sites indicate that the test section length was not sufficient to establish fully developed thermal conditions for V-shaped ribs with $p/e = 8$. Conversely, both *Nu*-distributions for V-shaped ribs with $p/e = 13.3$ seem to quickly attain the periodically developed thermal regime.

Further insights of the flow and heat transfer features can be inferred from inspection of Fig. 9 ($Re = 28{,}500$) where Nusselt number distributions over the central

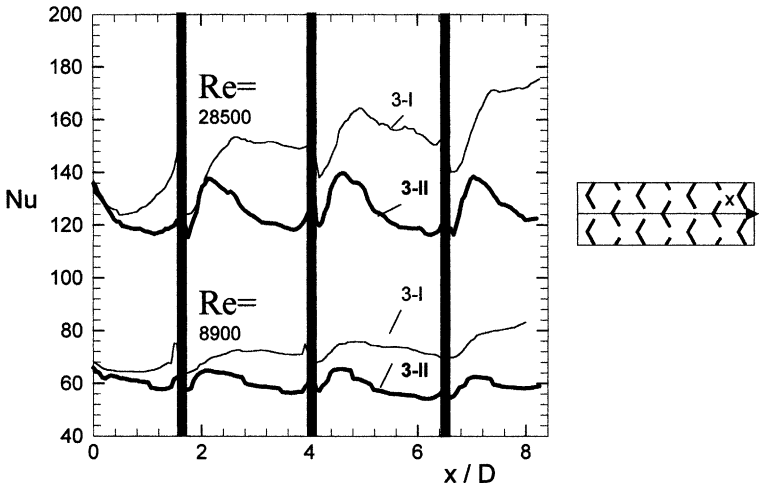


Fig. 7. Distributions of center-line Nusselt number for the 60 deg broken, V-shaped rib configurations 3-I ($p/e = 8$) and 3-II ($p/e = 13.3$), for $Re = 8900$ and 28,500.

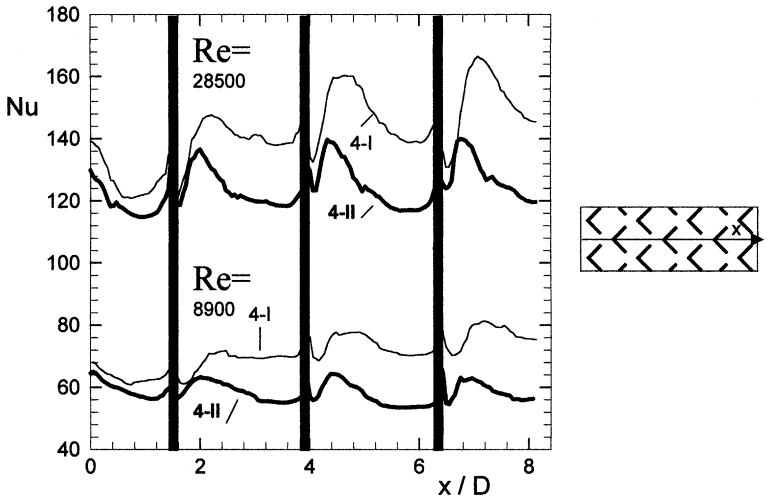


Fig. 8. Distributions of center-line Nusselt number for the 45 deg broken, V-shaped rib configurations 4-I ($p/e = 8$) and 4-II ($p/e = 13.3$), for $Re = 8900$ and 28,500.

region of the heated surface are plotted. Fig. 9(a) shows the *Nu* pattern for transverse, continuous ribs with $p/e = 8$. As expected, iso-*Nu* lines are almost parallel just downstream of the ribs while they are probably affected by weak secondary flows close to the lateral walls in the second part of the inter-rib space. In the presence of transverse, broken ribs, two main features dominate the heat transfer process: (i) the effect of vortices generated by the rib-endwall interaction and (ii) the flow separation and reattachment in the region downstream of ribs. A glance at Fig. 9(b), obtained for $p/e = 8$, shows that regions of surface having the highest heat transfer performance extend from the two rib edges and converge towards the axis normal to the rib. A similar pattern of *Nu*-lines, pictured in Fig. 9(c),was found for $p/e = 13.3$. It was deemed that the presence of V-shaped ribs induces pairs of counter-rotating cells in the part of the fluid climbing over the ribs, that produce high heat transfer coefficients in the downwash region between two successive apices of V-ribs. The remaining part of the fluid is driven by the angled legs towards the open spaces between adjacent V-ribs; vortex structures, generated at the rib leg extremities and entrained towards the V-rib bisector, are responsible for the two lobes of high magnitude of the heat transfer coefficient, as shown in Fig. 9(d) for the 60 deg V-shaped ribs with $p/e = 8$.

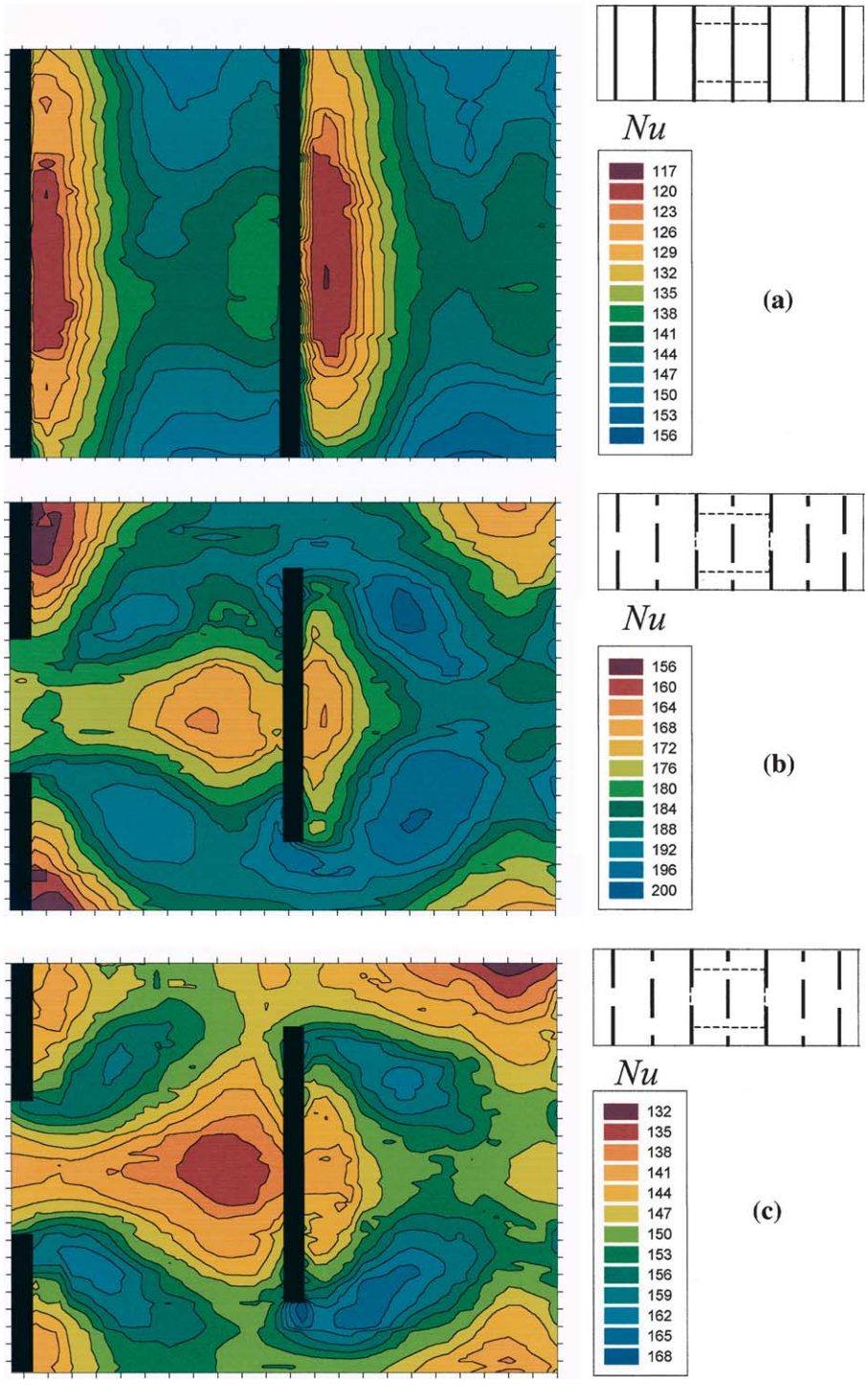


Fig. 9. Map of Nusselt number over the central (inline) region of the heated surface ($Re = 28500$): (a) transverse continuous ribs 1-I, (b) 90 deg broken ribs 2-I, (c) 90 deg broken ribs 2-II, (d) 60 deg V-shaped ribs 3-I, (e) 60 deg V-shaped ribs 3-II, (f) 45 deg V-shaped ribs 4-I.

A different pattern was found for V-shaped ribs at the same angle but with different rib height ($p/e = 13.3$, Fig. 9(e)). Here, the dominant role is played by the counter-rotating cells, and relative maxima in $Nu$-values occur

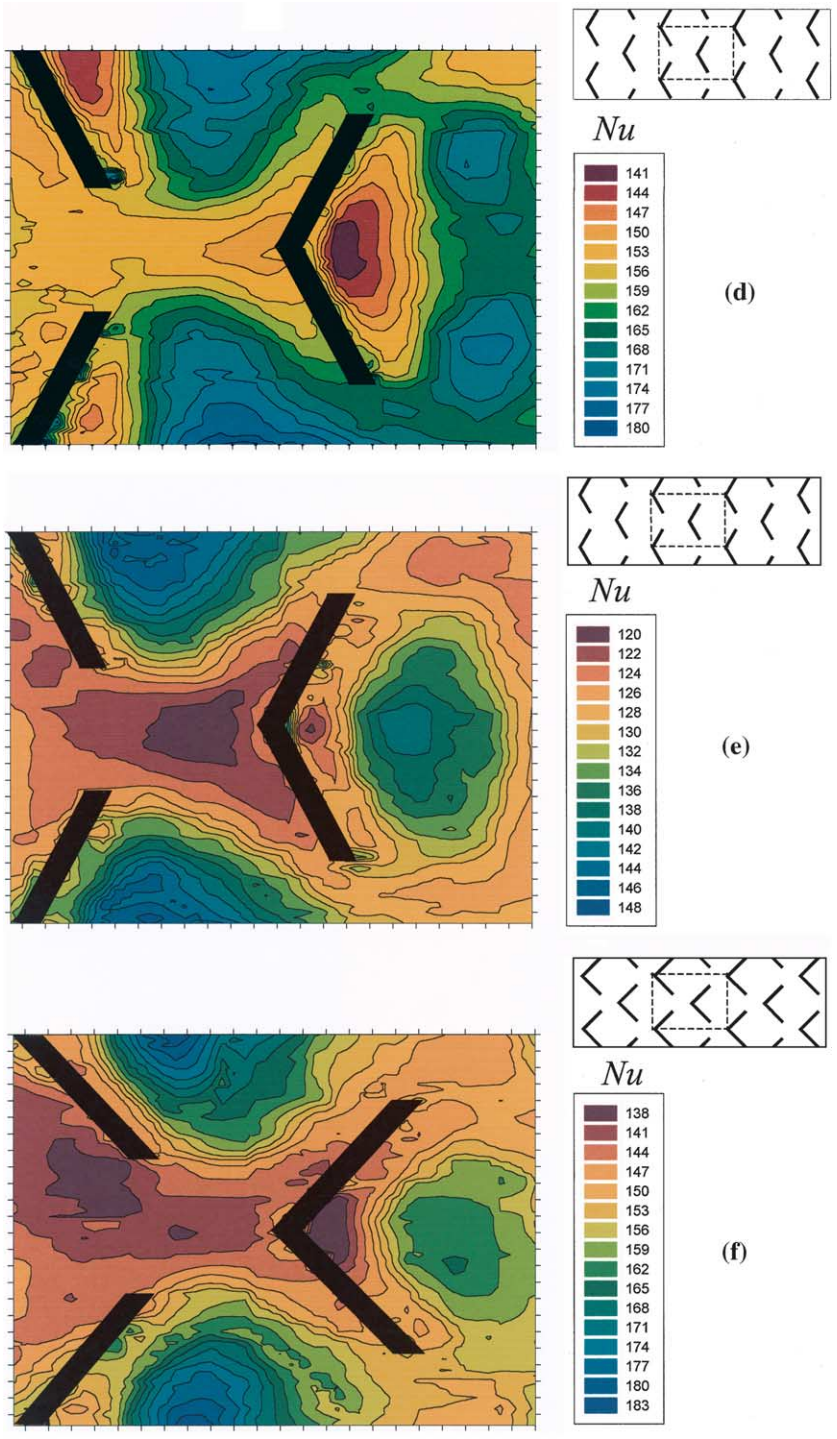


Fig. 9 (*continued*)

downstream of each V-rib apex. As the angle between the rib legs and the longitudinal coordinate is reduced (45 deg V-shaped ribs), local maxima in the heat transfer coefficient are present downstream of each V-rib apex for $p/e = 8$ (Fig. 9(f)) as well as for $p/e = 13.3$ (not shown for the sake of brevity).

### 3.2. Average heat transfer and friction characteristics

The average Nusselt number $Nu_{av}$ was calculated by averaging the local $h$ values and applying Eq. (4). In order to minimise the edge, inlet and outlet effects on the average heat transfer coefficient, $h$ values were averaged over a surface area 0.08 m wide and 0.21 m long, thus excluding the regions close to lateral boundaries and to the inlet/outlet sections. Thus calculated, the average Nusselt number is typically 0–4% lower than that computed by considering the entire test surface (0.10 m wide, 0.28 m long).

Results are plotted in Fig. 10 together with some literature relationships valid for asymmetrically heated rectangular channels and smooth tubes with fully developed flow conditions [24–27]. Symbols refer to experimental data obtained for ribbed surfaces and to the values recorded for the test surface without ribs (smooth channel) at a streamwise location $x/D = 8$. The spread between Nusselt numbers given by literature relationships (lines in the figure) for smooth channels/tubes is quite large. Experimental data for the unribbed surface show satisfactory agreement with Dittus–Boelter equation, even though it tends to overestimate the average Nusselt number for a channel with an asymmetrical heating by 10–20% [25]. This can be explained by pointing out that experimental data for the unribbed surface, although recorded as far as possible from the inlet section ($x/D = 8$), do not correspond to fully developed thermal conditions.

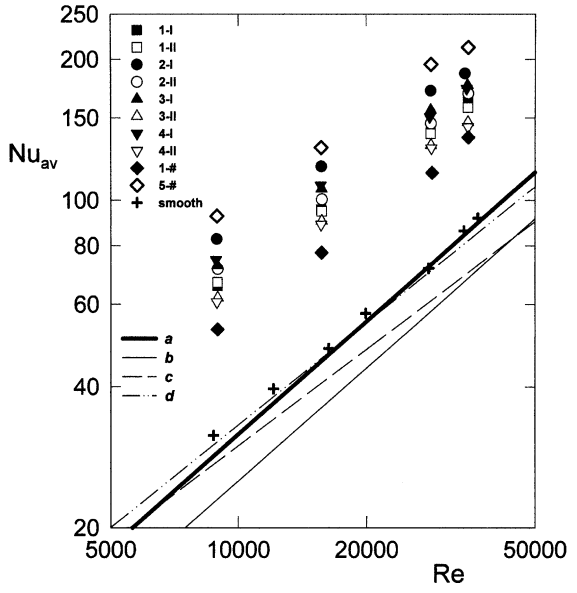


Fig. 10. Average Nusselt number for the rib configurations (open and closed symbols) and Nusselt number at $x/D = 8$ for the smooth channel (cross symbols). **a–d**: typical correlations for the fully developed flow Nusselt number in the smooth channel: **a**: $Nu_0 = 0.023Re^{0.8}Pr^{0.4}$; **b**: $Nu_0 = 0.019Re^{0.8}Pr^{0.5}$; **c**: $Nu_0 = 0.055Re^{0.684}$ ($Pr = 0.7$); **d**: $Nu_0 = 0.041Re^{0.727}$ ($Pr = 0.7$).

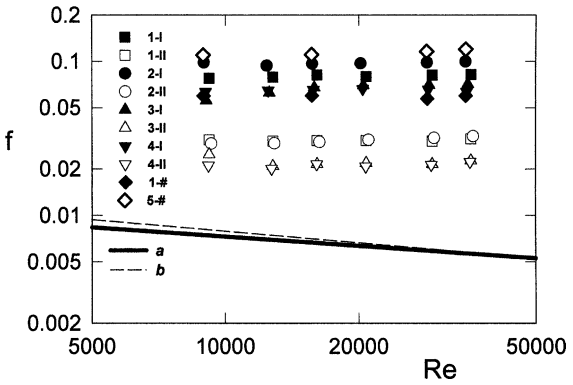


Fig. 11. Friction factor for the rib configurations, a–b typical correlations for smooth channels: **a**: $f = 0.046Re^{-0.2}$; **b**: $f = 0.079Re^{-0.25}$.

Inspection of the figure reveals that $Nu_{av}$ values for the ribbed channels are correlated to the Reynolds number by power laws having the exponent in the 0.61–0.67 range. Transverse broken ribs provide the highest average Nusselt numbers, with higher ribs ($e = 5$ mm, $p/e = 4$ and 8) performing better than lower ribs ($e = 3$ mm, $p/e = 13.3$). Transverse continuous ribs (with $p/e = 4$ and 8) lead to lower average heat transfer coefficients relative to transverse broken ribs (with $p/e = 4$ and 8) and to V-shaped ribs (with $p/e = 8$). For $p/e = 13.3$, transverse continuous ribs yield again lower Nusselt number values than 90 deg broken ribs but higher than the V-shaped ribs. Finally, the average Nusselt number was found to be practically insensitive to the angle of inclination for V-shaped ribs, at both $p/e$ values.

Friction factor ratio $f$, reported in Fig. 11 together with standard relationships for the reference smooth channel [26], is almost independent of the Reynolds number for all the ribbed configurations; as expected, large increases (from 2 to 21 times) in friction factor are induced by ribs, relative to the smooth channel, especially when ribs are tall ($e = 5$ mm), broken and transverse (90 deg broken ribs).

### 3.3. Performance evaluation criteria

Several performance comparison criteria for heat exchangers have been proposed in the literature (see for instance Refs. [28–30]). Bergles et al. [29] have suggested that the heat transfer from the enhanced surface (the endwall with ribs) can be compared with that from a reference surface (a smooth channel) according to given geometric and/or operating constraints. For instance the heat transfer augmentation provided by the enhanced geometry can be evaluated by keeping the mass flow rate constant or, alternatively, fixing the power required to pump the fluid (over the enhanced and reference surfaces).

For the purpose of comparison, the following relationships giving $Nu_0$ and $f_0$ for the fully developed turbulent flow in a duct have been considered for the (smooth) reference channel:

$$Nu_0 = 0.023 Re_0^{0.8} Pr^{0.4} \quad (7)$$

$$f_0 = 0.046 Re_0^{-0.2} \quad (8)$$

where $Re_0$ is the Reynolds number based on the mass flow rate passing through the reference channel.

Comparison of the heat transfer performance under the same mass flow rate implies that the Reynolds numbers $Re$ and $Re_0$ for the ribbed and smooth channels are equal to each other. The degree of heat transfer enhancement (relative to the smooth surface), expressed by the ratio between $Nu_{av}$ and $Nu_0$, is plotted in Fig. 12. As found by other Authors in similar studies [4,9,12, 15,16], $Nu_{av}/Nu_0$ tends to decrease as the Reynolds number increases. The highest values of $Nu_{av}/Nu_0$, obtained for the configuration **5-#** (transverse broken ribs with $p/e = 4$), are in the 2.4–3.2 range, followed by the configuration **2-I** (transverse broken ribs, $p/e = 8$), with $Nu_{av}/Nu_0$ between 2.2 and 2.9.

The quantity $Nu_{av}/Nu_0$ can be estimated according to the equal pumping-power performance criterion. In order to respect this constraint, the mass flow rates passing through the enhanced and reference channel cannot be the same; the assumption of constant pumping power leads to the following expression for the Reynolds numbers:

$$Re_0 = (21.74 f Re^3)^{0.357} \quad (9)$$

where $Re_0$ is the value of the Reynolds number to be used in Eq. (7) to evaluate $Nu_0$. The value of $Nu_{av}/Nu_0$ reported in Fig. 13 (where the ascissa $Re_0$ was chosen as a convenient reference for all the ribbed channels) can determine whether or not a given surface is potentially

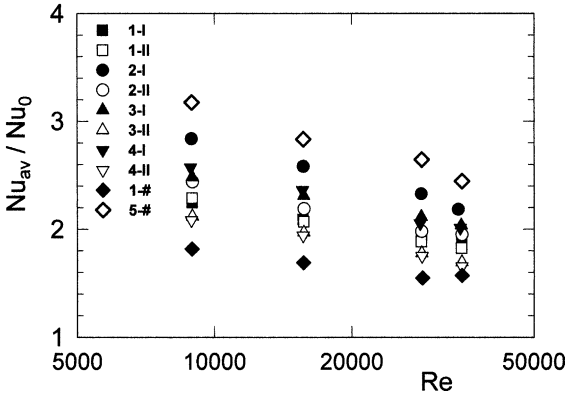


Fig. 12. Ratio of average Nusselt number with and without ribs against the Reynolds number for fixed mass flow rates.

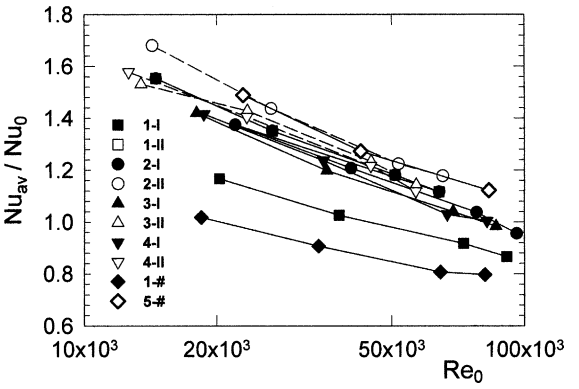


Fig. 13. Ratio of average Nusselt number with and without ribs against the reference Reynolds number for fixed pumping powers.

advantageous under the requirement that the pumping power must be the same. This criterion is similar to that employed in [28], where the group $(St/St_0)/(f/f_0)^{1/3}$ ($St$ being the Stanton number) was used to quantify the thermal performance; the only difference is that in [28] the equal mass flow rate constraint implies different flow areas for ribbed and for smooth passages. According to the results shown in Fig. 13, the degree of the heat transfer enhancement (up to 1.7) is lower than that obtained for the fixed mass flow rate constraint. The thermal performance of configurations **2-II** (transverse broken ribs with $p/e = 13.3$) is about the same as the configuration **5-#** (transverse broken ribs with $p/e = 4$), while transverse continuous ribs with $p/e = 4$ and 8 lead to a slight heat transfer augmentation or even to a reduction relative to the reference channel. All the other configurations provide a similar thermal performance with heat transfer enhancements in the 1.0–1.6 range, depending on the Reynolds number $Re_0$.

## 4. Conclusions

Liquid crystal thermography has been used to obtain detailed distributions of the heat transfer coefficient in rib-roughened channels. The heat transfer modifications induced by transverse continuous, transverse broken and V-shaped broken ribs, periodically deployed on a heated surface, were observed. Based on the results, conclusions are the following:

- features of the inter-rib distributions of the heat transfer coefficient are strongly related to rib shape and geometry; a relative maximum is typically attained downstream of each rib for continuous transverse ribs (due to flow reattachment), 45 deg V-shaped ribs (both $p/e$ values) and 60 deg V-shaped ribs

at $p/e = 13.3$ (due to double-cell counter-rotating vortices);

- when ribs are transverse and broken (or 60 deg V-shaped with $p/e = 8$), pairs of high heat transfer coefficient lobes are located aside the line normal to ribs (when transverse) or aside the bisector of ribs (when V-shaped) due to the high turbulence levels produced by rib tip–endwall interactions;
- a periodically, fully developed thermal field is quickly attained for transverse continuous ribs (at both $p/e$ values) and V-shaped broken ribs having the lower height ($e = 3$ mm, $p/e = 13.3$); in the remaining cases, inter-rib $h$ profiles are almost repetitive in shape but the average value tends to increase in the direction of the main flow;
- transverse broken ribs with $p/e = 4$ and 8 give the higher heat transfer augmentation (relative to the reference smooth channel) under the same mass flow rate constraint; when pressure drop is taken into account (fixed pumping power constraint), transverse broken ribs with $p/e = 4$ and 13.3 have the best thermal performance, while transverse continuous ribs (again with $p/e = 4$ and 8) provide a little heat transfer augmentation or even a reduction.

## References

[1] D. Wilkie, Forced convection heat transfer from surfaces roughened by transverse ribs, Proceedings of the Third International Heat Transfer Conference, vol.1, Chicago, USA, 1966, pp. 1–19.
[2] E.M. Sparrow, W.Q. Tao, Enhanced heat transfer in a flat rectangular duct with streamwise-periodic disturbances at one principal wall, ASME J. Heat Transfer 105 (1983) 851–861.
[3] J.C. Han, Heat transfer and friction in channels with two opposite rib-roughened walls, ASME J. Heat Transfer 106 (1984) 774–781.
[4] J.C. Han, Heat transfer and friction characteristics in rectangular channels with rib turbulators, ASME J. Heat Transfer 110 (1988) 321–328.
[5] L. White, D. Wilkie, The heat transfer and pressure loss characteristics of some multi-stard ribbed surfaces, in: A.E. Bergles, R.L. Webb (Eds.), Augmentation of Convective Heat and Mass Transfer, ASME, New York, 1970.
[6] J.C. Han, L.R. Glickmann, W.M. Rohsenow, An investigation of heat transfer and friction for rib-roughened surfaces, Int. J. Heat Mass Transfer 21 (1978) 1143–1156.
[7] J.C. Han, J.S. Park, C.K. Lei, Heat transfer enhancement in channels with turbulence promoters, ASME J. Eng. Gas Turbines Power 107 (1985) 628–635.
[8] J.C. Han, J.S. Park, Developing heat transfer in rectangular channels with rib turbulators, Int. J. Heat Mass Transfer 31 (1988) 183–195.
[9] J.C. Han, S. Ou, J.S. Park, C.K. Lei, Augmented heat transfer in rectangular channels of narrow aspect ratios with rib turbulators, Int. J. Heat Mass Transfer 32 (1989) 1619–1630.
[10] D.L. Gee, R.L. Webb, Forced convection heat transfer in helically rib-roughened tubes, Int. J. Heat Mass Transfer 23 (1980) 1127–1136.
[11] R. Sethumadhavan, M. Raja Rao, Turbulent flow heat transfer and fluid friction in helical-wire-coil-inserted tubes, Int. J. Heat Mass Transfer 26 (1983) 1833–1844.
[12] J.C. Han, Y.M. Zhang, C.P. Lee, Augmented heat transfer in square channels with parallel, crossed, and V-shaped angled ribs, ASME J. Heat Transfer 113 (1991) 590–596.
[13] R.T. Kukreja, S.C. Lau, R.D. McMillin, Local heat/mass transfer distribution in a square channel with full and V-shaped ribs, Int. J. Heat Mass Transfer 36 (1993) 2013–2020.
[14] X. Gao, B. Sundén, Heat transfer distribution in rectangular ducts with V-shaped ribs, Heat Mass Transfer 37 (2001) 315–320.
[15] J.C. Han, Y.M. Zhang, High performance heat transfer ducts with parallel broken and V-shaped broken ribs, Int. J. Heat Mass Transfer 35 (1992) 513–523.
[16] S.V. Ekkad, J.C. Han, Detailed heat transfer distributions in two-pass square channels with rib turbulators, Int. J. Heat Mass Transfer 40 (1997) 2525–2537.
[17] T.-M. Liou, C.-C. Chen, T.-W. Tsai, Heat transfer and fluid flow in a square duct with 12 different shaped vortex generators, ASME J. Heat Transfer 122 (2000) 327–335.
[18] D. Cavallero, G. Tanda, An experimental investigation of forced convection heat transfer in channels with rib turbulators by using the liquid crystal thermography, Exp. Thermal Fluid Sci. 26 (2002) 115–121.
[19] D. Aliaga, J.P. Lamb, D.E. Klein, Convective heat transfer distributions over plates with square ribs from infrared thermography measurements, Int. J. Heat Mass Transfer 37 (1994) 363–374.
[20] A. Valencia, M. Fiebig, N.K. Mitra, Influence of heat conduction on determination of heat transfer coefficient by liquid crystal thermography, Exp. Heat Transfer 8 (1995) 271–279.
[21] C. Camci, K. Kim, S.A. Hippensteele, A new hue capturing technique for the quantitative interpretation of liquid crystal images used in convective heat transfer studies, ASME J. Turbomach. 114 (1992) 765–775.
[22] J.W. Baughn, M.R. Anderson, J.E. Mayhew, J.D. Wolf, Hysteresis of thermochromic liquid crystal temperature measurement based on hue, ASME J. Heat Transfer 121 (1999) 1067–1072.
[23] R.J. Moffat, Describing the uncertainties in experimental results, Exp. Thermal Fluid Sci. 1 (1988) 3–17.
[24] A.P. Hatton, A. Quarmby, I. Grundy, Further calculations on the heat transfer with turbulent flow between parallel plates, Int. J. Heat Mass Transfer 7 (1964) 817–823.
[25] E.M. Sparrow, J.R. Lloyd, C.W. Hixon, Experiments on turbulent heat transfer in an asymmetrically heated rectangular duct, ASME J. Heat Transfer 88 (1966) 170–174.
[26] A. Bejan, Heat Transfer, J. Wiley & Sons, New York, 1993.
[27] R. Matsumoto, S. Kikkawa, M. Senda, Effect of pin fin arrangement on endwall heat transfer, JSME Int. J., Ser. B 40 (1997) 142–151.

[28] R.L. Webb, E.R.G. Eckert, Application of rough surfaces to heat exchanger design, Int. J. Heat Mass Transfer 15 (1972) 1647–1658.
[29] A.E. Bergles, A.R. Blumenkrantz, J. Taborek, Performance evaluation criteria for selection of enhanced heat transfer surfaces, Proceedings of the 5th Heat Transfer Conference, vol. 2, Tokyo, Japan, 1974, pp. 239–243.
[30] L. Tagliafico, G. Tanda, A thermodynamic method for the comparison of plate-fin heat exchanger performance, ASME J. Heat Transfer 118 (1996) 805–809.